Near-field optical studies of semicontinuous metal films

S. Ducourtieux,[1] V. A. Podolskiy,[2] S. Grésillon,[1] S. Buil,[1] B. Berini,[3] P. Gadenne,[3] A. C. Boccara,[1] J. C. Rivoal,[1]
W. A. Bragg,[2] K. Banerjee,[2] V. P. Safonov,[4] V. P. Drachev,[5] Z. C. Ying,[2] A. K. Sarychev,[2] and Vladimir M. Shalaev[6]

[1]*CNRS UPR A0005 et Université P. et M. Curie, Laboratoire d'Optique Physique, ESPCI, 75231 Paris Cedex 05, France*
[2]*Department of Physics, New Mexico State University, Las Cruces, NM 88003*
[3]*LMOV, Université de Versailles Saint-Quentin, 78035 Versailles, France*
[4]*Institute of Automation and Electrometry, Novosibirsk 630090, Russia*
[5]*Institute of Semiconductor Physics, Novosibirsk 630090, Russia*
[6]*School of Electrical and Computer Engineering, Purdue University, West Lafayette, Indiana 47907-1285*

Local field distributions in random metal-dielectric films near a percolation threshold are experimentally studied using scanning near-field optical microscopy (SNOM). The surface-plasmon oscillations in such percolation films are localized in small nanometer-scale areas, "hot spots," where the local fields are much larger than the field of an incident electromagnetic wave. The spatial positions of the hot spots vary with the wavelength and polarization of the incident beam. Local near-field spectroscopy of the hot spots is performed using our SNOM. It is shown that the resonance quality-factor of hot spots increases from the visible to the infrared. Giant *local* optical activity associated with chiral plasmon modes has been obtained. The hot spot's large local fields may result in local, frequency and spatially selective photomodification of percolation films.

I. INTRODUCTION

Metal-dielectric composites attract much attention because of their unique optical properties, which are significantly different from those of constituents forming the composite.[1–9] In our recent paper[10] we showed that plasmon modes in metal-dielectric films near the percolation threshold (referred in this case as to semicontinuous metal films) are localized in small nanometer-scale areas, "hot spots." The localization was attributed to Anderson localization of plasmons. The electromagnetic energy is accumulated in the hot spots associated with the localized plasmons, leading to the local fields that can exceed the intensity of the applied field by four to five orders of magnitude. In Ref. 11 we developed a theory of nonlinear optical responses in percolation composites; these nonlinearities are dramatically enhanced by the localized plasmons. The theory[11] has further developed our earlier considerations of optical properties of metal-dielectric films[12–15] (for review, see Refs. 16 and 17).

Semicontinuous metal films can be produced, for example, by thermal evaporation or sputtering of metal onto an insulating substrate. In the growing process, first, small metallic grains are formed on the substrate. A typical size a of a metal grain can vary from 5 to 50 nm. As the film grows, the metal filling factor increases and coalescence occurs, so that irregularly shaped self-similar clusters (fractals) are formed on the substrate. The concept of scale invariance (fractality) plays an important role in description of various properties of percolation systems.[16–19] The sizes of the fractal structures diverge in the vicinity of the percolation threshold, where an infinite percolation cluster of metal is eventually formed, representing a continuous conducting path between the ends of a sample. At the percolation threshold the metal-insulator transition occurs in the system. At higher surface coverage, the film is mostly metallic, with voids of irregular shape. With a further coverage increase the film becomes uniform.

Metal-dielectric films exhibit anomalous optical phenomena that are absent for bulk metal and dielectric components. For example, the anomalous absorption in the near-infrared spectral range leads to unusual behavior of the transmittance and reflectance of the film.[20–25] A number of effective-medium theories were proposed for calculation of the optical properties of random films, including the Maxwell-Garnett and Bruggeman approaches and their various modifications;[2,22,23,26] these approaches, however, do not allow one to calculate the local fields, experiencing giant spatial fluctuations associated with the existence of the hot spots. A theory for the local-field distribution in percolation films has been developed in Refs. 11,12,14–17 and it was experimentally verified in Ref. 10.

The local electromagnetic field fluctuations are especially strong in the optical and infrared spectral ranges because of the localized plasmon oscillations. Quality factors of these plasmon resonances can be very large in metal-dielectric composites, where the dielectric constant ϵ_m for a metallic component is such that the real part is negative, $\epsilon'_m < 0$, and can be large in magnitude, whereas the imaginary part ϵ''_m is positive and relatively small, $\kappa = \epsilon''_m / |\epsilon_m| \ll 1$.[11–13]

Since the metal-insulator transition associated with percolation represents a geometrical phase transition one might anticipate that the current and field fluctuations are scale invariant and large, in this case. In percolation composites, however, the fluctuation pattern appears to be quite different from that for a second-order phase transition, where fluctuations are characterized by a long-range correlation and their relative magnitudes are of the order of unity at any point. In contrast, for the dc percolation, for example, the local electric fields are concentrated at the edges of large metal clusters so that the field maxima (large fluctuations) are separated by distances of the order of the percolation correlation length ξ which diverges when the metal concentration ap-

64 1554XX-1

proaches the percolation threshold p_c.[18]

As shown in our recent publications[10–14] the difference in fluctuations becomes even more striking for the ac response in the optical spectral range where the local-field peaks have a resonance nature and, therefore, their relative magnitudes can be up to 10^5, for the linear response, and up to 10^{20} and more for nonlinear responses (e.g., for a third-order optical nonlinearity), with distances between the peaks ξ_e that can be significantly different from the percolation length ξ.

Scanning near-field optical microscopy (SNOM), with its sub-wavelength resolution, allows the detecting of nm-sized field peaks in fractal aggregates[27,28] and on rough metal surfaces.[29,30] In our first report[10] we have also demonstrated that SNOM can be successfully employed for studying localized plasmon oscillations in metal-dielectric composites.

In the present paper, we report results of our experimental study of local field distributions on percolation metal-dielectric films, using our SNOM providing one of the best reported spatial resolutions, about 10 nm. This allowed us to detect the hot spots localized in the areas as small as 10 nm, with much stronger enhancement than previously observed in Ref. 10. We present here results of our detailed spectroscopic studies of the hot spots. In particular, we compare the spectral properties in the visible and near-infrared parts of the spectrum. The observed spectral and polarization dependence of plasmon oscillations are compared with theoretical simulations.

We also report here a new effect of giant *local* optical activity in percolation films. This effect occurs only locally and can be detected in SNOM measurements; the macroscopic optical activity disappears (or becomes very small) in the far zone of a percolation film. This is because the plasmon modes can be chiral active when probed individually; however, because of the modes' different handedness, they cancel each other out when the *macroscopic* optical activity is probed.

In Sec. II, we briefly recapitulate basic ideas and results of our general theory[11] for the field distribution in percolation films, using a simple approach. In contrast to rigorous but rather complicated considerations of Ref. 11, here we provide a simple qualitative description of our theory, which we believe is clear and well suited to guide the current and future experimental studies in the field. The main Sec. III discusses our near-field optical studies of semicontinuous metal films. All experimental observations described here are accompanied by complementary numerical simulations. Finally, Sec. IV summarizes the results obtained and concludes the paper.

II. LOCAL-FIELD DISTRIBUTION: THEORY OUTLINE

Below we consider main properties of the field distribution on a two-dimensional percolation film, using a simple qualitative approach. These considerations then will be employed to interpret our experimental observations described in the next section.

For the films concerned, gaps between metal grains are filled by a dielectric substrate so that a semicontinuous metal film can be thought of as a two-dimensional (2D) array of metal and dielectric grains randomly distributed over the plane. The dielectric constant of a metal can be approximated by the Drude formula

$$\epsilon_m = \epsilon_b - (\omega_p/\omega)^2/(1 + i\omega_\tau/\omega), \tag{1}$$

where ϵ_b is the interband contribution, ω_p is the plasma frequency, and ω_τ is the plasmon relaxation rate ($\omega_\tau \ll \omega_p$). In the high-frequency range considered here, losses in metal grains are relatively small, $\omega_\tau \ll \omega$. Therefore, the real part ϵ'_m of the metal dielectric function ϵ_m is much larger (in modulus) than the imaginary part ϵ''_m, i.e., the loss parameter κ is small, $\kappa = \epsilon''_m/|\epsilon'_m| \cong \omega_\tau/\omega \ll 1$. We note that ϵ'_m is negative for frequencies ω less than the renormalized plasma frequency, $\widetilde{\omega}_p = \omega_p/\sqrt{\epsilon_b}$.

It is instructive to consider first the special case of $-\epsilon'_m = \epsilon_d$, where $\epsilon_m \equiv |\epsilon'_m|(-1 + i\kappa)$ and ϵ_d are the dielectric constants of the metallic and dielectric components of the composite, respectively. The condition $-\epsilon'_m = \epsilon_d$ corresponds to the resonance of individual metal particles in a dielectric host, in the two-dimensional case. For simplicity, we also set $-\epsilon_m = \epsilon_d = 1$, which can always be done simply renormalizing the corresponding quantities.

It can be shown that the field distribution on a percolation film at $-\epsilon_m = \epsilon_d = 1$ formally maps the Anderson metal-insulator transition problem.[10,11,16,17] In accord with this, the field potential representing plasmon modes of a percolation film must be characterized by the same spatial distribution as the electron wave function in the Anderson transition problem. Such mathematical equivalence of the two physically different problems stems from the fact that the current conservation law for a percolation film, acquires (when written in the discretized form) the form of the Kirchhoff's equations, which, in turn (when written in the matrix form), become identical to the equations describing the Anderson transition problem.[11] The corresponding Kirchhoff Hamiltonian for the field-distribution problem is given by a matrix with random elements which can be expressed in terms of the dielectric constants for metallic and dielectric bonds of the lattice representing the film. In this matrix, the values $\epsilon_m = -1$ and $\epsilon_d = 1$ appear in the matrix elements with probability p and $(1-p)$, respectively (where p is the metal filling factor given at percolation by $p = p_c$, with $p_c = 1/2$ for a self-dual system). In such a form, the Kirchhoff Hamiltonian is characterized by the random matrix, similar to that in the Anderson transition problem, with both on- and off-diagonal disorder. Based on this mathematical equivalence, it was concluded in Refs. 10,11,16,17 that the plasmons in a percolation film can experience the Anderson-type localization within small areas, with the size given by the Anderson length ξ_A. For the most localized plasmon modes ξ_A can be as small as the size of one grain a.

Below we develop a simple scaling approach that explains the nontrivial field distribution predicted and observed in percolation films. This scale-renormalization method supports the main conclusions of a rigorous (but tedious) theory of Refs. 11,17 and has a virtue of being simple and clear, which is important for understanding and interpretation of future experiments.

First, we estimate the field in the hot spots for the considered case of $-\epsilon'_m = \epsilon_d$. Hereafter we use the asterisk (not to be confused with complex conjugation) to indicate that the quantity concerned is given for the considered case of $-\epsilon'_m = \epsilon_d \sim 1$; for ξ_A, however, we omit this sign since this quantity always refers to the case of $-\epsilon'_m = \epsilon_d$.

Since at the optical frequencies ϵ'_m is negative, metal particles can be roughly thought of as inductor-resistor (L-R) elements, whereas the dielectric gaps between the particles can be treated as capacitive (C) elements. Then, the condition $\epsilon'_m = -\epsilon_d$ means that the conductivities of the L-R and C elements are equal in magnitude and opposite in sign, i.e., there is a resonance in the equivalent L-R-C circuit corresponding to individual particles.

The local field in resonating particles is enhanced by the resonance quality-factor Q which is the inverse of the loss factor, $Q = \kappa^{-1}$, so that $E^*_m \sim E_0 \kappa^{-1}(a/\xi_A)^2$, where the factor $(a/\xi_A)^2$ takes into account that the resonating mode is localized within ξ_A. The resonant modes excited by a monochromatic light represent only the fraction κ of all the modes so that the average distance (referred to as the field correlation length ξ^*_e) between the field peaks is given by $\xi^*_e \sim a/\sqrt{\kappa} \gg \xi_A$.

Note that the field peaks associated with the resonance plasmon modes represent in fact the normal modes, with the near-zero eigennumbers, of the Kirchhoff's Hamiltonian discussed above.[11] These modes are strongly excited by the applied field and seen as giant field fluctuations on the surface of the film.

Now we turn to the important case of the "high contrast," with $|\epsilon_m| \gg \epsilon_d$, that corresponds to the long-wavelength part of the spectrum where the local-field enhancement can be especially strong. From basic principles of Anderson localization,[17] it is clear that a higher contrast favors localization so that plasmon modes are expected to be localized in this case as well.

It is clear that at $|\epsilon_m| \gg \epsilon_d$ individual metal particles cannot resonate. We can renormalize, however, the high-contrast system to the case of $-\epsilon'_m = \epsilon_d$ considered above. We divide a system into squares of size l and consider each square as a new renormalized element. All such squares can be classified into two types. A square is considered as a "conducting" element if the square contains a continuous path of metallic particles that spans it in "x" or "y" direction. A square without such an "infinite" cluster is considered as a nonconducting, "dielectric," element. According to finite size scaling[2,18] the effective dielectric constant of the "conducting" square $\varepsilon_m(l)$ decreases with increasing its size l as $\varepsilon_m(l) \simeq (l/a)^{-t/\nu} \varepsilon_m$, whereas the effective dielectric constant of the "dielectric" square $\varepsilon_d(l)$ increases with l as $\varepsilon_d(l) \simeq (l/a)^{s/\nu} \varepsilon_d$ (t, s, and ν are the percolation critical exponents for the static conductivity, dielectric constant, and percolation correlation length, respectively; for the 2D case, $t \cong s \cong \nu \cong 4/3$). Now, we set the square size l to be equal to

$$l = l_r = a(|\varepsilon_m|/\varepsilon_d)^{\nu/(t+s)} \simeq a\sqrt{|\varepsilon_m|/\varepsilon_d}. \tag{2}$$

Then, in the renormalized system, where each square of the size l_r is considered as a single element, the dielectric con-

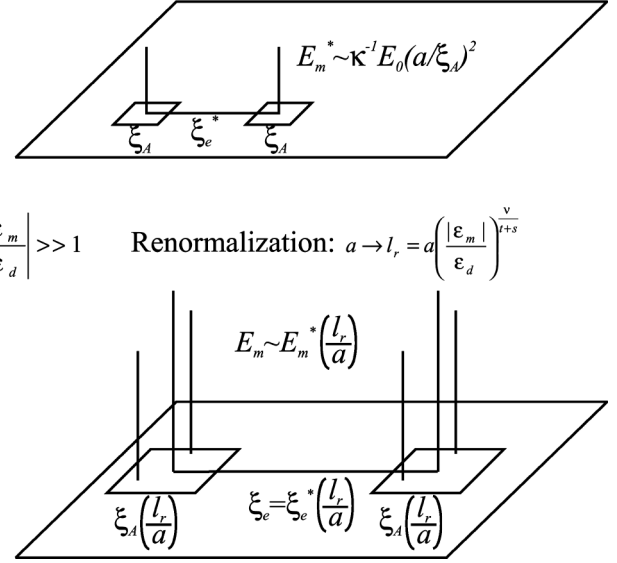$\epsilon_d = -\epsilon_m = 1$

FIG. 1. Renormalization of the field distribution at transition from the reference system with $-\epsilon_m/\epsilon_d = 1$ to the high-contrast system with $-\epsilon_m/\epsilon_d \gg 1$.

stant of these new elements takes either value $\varepsilon_m(l_r) = \varepsilon_d^{t/(t+s)}|\varepsilon_m|^{s/(t+s)}(\varepsilon_m/|\varepsilon_m|)$, for the element renormalized from the conducting square, or $\varepsilon_d(l_r) = \varepsilon_d^{t/(t+s)}|\varepsilon_m|^{s/(t+s)}$, for the element renormalized from the dielectric square. The ratio of the dielectric constants of these new elements is equal to $\varepsilon_m(l_r)/\varepsilon_d(l_r) = \varepsilon_m/|\varepsilon_m| \cong -1 + i\kappa$. Thus, for these renormalized elements of the size l_r, there is a resonance similar to the resonance in the R-L-C circuit describing individual metal particles in a dielectric host. In this case, however, some effective (renormalized) R-L-C circuits represent the resonating square elements.

In the renormalized system, the estimate obtained above for field peaks still holds. Since the electric field and eigenfunction both scale as l_r we arrive at the conclusion that in the high-contrast system (with $|\epsilon_m| \gg \epsilon_d$), the field maxima are estimated as $E_m \sim (l_r/a)E^*_m \sim E_0 \kappa^{-1}(l_r/a)(a/\xi_A)^2$, i.e., as

$$E_m/E_0 \sim (a/\xi_A)^2 |\epsilon_m|^{3/2}/(\epsilon_d^{1/2}\epsilon''_m). \tag{3}$$

The light-induced eigenmodes in the high-contrast system are separated, on average, by the distance ξ_e that exceeds the mode separation ξ^*_e at $\epsilon_m = -\epsilon_d$ by factor l_r/a, so that $\xi_e \sim (l_r/a)\xi^*_e \sim l_r/\sqrt{\kappa}$ or

$$\xi_e \sim a|\epsilon_m|/\sqrt{\epsilon''_m \epsilon_d}. \tag{4}$$

For a Drude metal at $\omega \ll \omega_p$, the local field peaks, according to Eqs. (1) and (3) are given by $E_m/E_0 \sim \epsilon_d^{-1/2}(a/\xi_A)^2(\omega_p/\omega_\tau)$, and the distance between the excited modes (4) is estimated as $\xi_e \sim a\omega_p/\sqrt{\epsilon_d \omega \omega_\tau}$.

Figure 1 illustrates the described above renormalization of the field peaks and their spatial separations at the transition between the reference (renormalized) system with $-\epsilon_m$
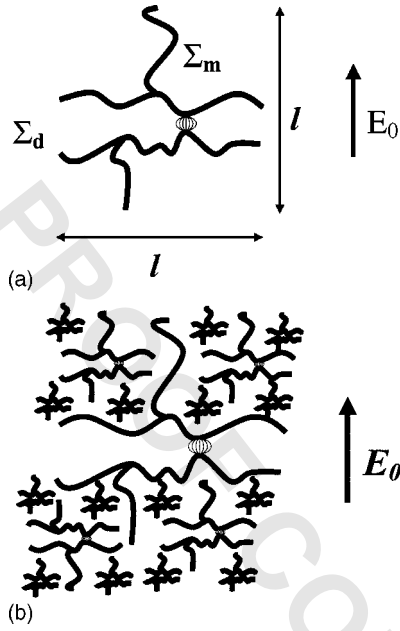
FIG. 2. (a) A typical element of a percolation film consisting of two conducting metal clusters with a dielectric gap in between. (b) Different resonating elements of a percolation film at different wavelengths.

$=\epsilon_d=1$ and the high-contrast system of $|\epsilon_m/\epsilon_d|\gg 1$. As follows from the figure, largest local fields of the amplitude E_m result from excitation of the resonant clusters of the size l_r. At $-\epsilon_m=\epsilon_d=1$, we have $l_r=a$ [see Eq. (2)], as in the reference system. With increasing the wavelength (and thus the contrast $|\epsilon_m|/\epsilon_d$), the resonant size l_r and distance ξ_e between the resonating modes both increase.

The above results have a clear physical interpretation and can be also obtained from the following simple considerations. Let us consider two metal clusters, with conductance $\Sigma_m=-i(a/4\pi)\omega\epsilon_m(l)$, separated by a dielectric gap, with the conductance $\Sigma_d=-i(a/4\pi)\omega\epsilon_d(l)$, as shown in Fig. 2(a). The clusters and the gap are both of a size l, and $\epsilon_m(l)$ and $\epsilon_d(l)$ for the finite size elements are defined above. The equivalent conductance Σ_e for Σ_m and Σ_d in series is given by $\Sigma_e=\Sigma_m\Sigma_d/(\Sigma_m+\Sigma_d)$ and the current j through the system is $j=\Sigma_e E_0 l$. The local field, however, is strongly inhomogeneous and the largest field occurs at the point of the close approach between the clusters, where the separation between clusters can be as small as a; then, the maximum field E_m is estimated as $E_m=(j/\Sigma_d)/a\sim E_0(l/a)/[1+(l/a)^{(t+s)/\nu}\epsilon_d/\epsilon_m]$. For the "resonant" size $l=l_r$, the real part of the denominator in the expression for E_m becomes zero, and the field E_m reaches its maximum, where it is estimated as $E_m/E_0\sim\kappa^{-1}(l_r/a)$.

In the obtained estimate we assumed, for simplicity, that $\xi_A\sim a$ and, in this limit, we reproduced the result (3). In order to obtain the "extra factor" $(a/\xi_A)^2$ of Eq. (3), we have to take into account that the localization area for the field is ξ_A rather than a, so that the field peak is "spread" over the distance ξ_A. With this correction we immediately arrive at the formula (3).

It is clear that for any frequency of the applied field ω

there are always resonant clusters of the size (2) $l=l_r(\omega)\sim a(\tilde{\omega}_p/\omega)^{2\nu/(t+s)}$, where the local field reaches its maximum E_m. The resonant size l_r increases with the wavelength. It is important that at percolation, the system is scale invariant so that all possible sizes needed for the resonant excitation are present, as schematically illustrated in Fig. 2(b). At some large wavelength, only large clusters of appropriate sizes resonate leading to field peaks at the points of close approach between the metal clusters; with the decrease of the wavelength of the applied field, the smaller clusters begin to resonate, whereas the larger ones are off the resonance [see Fig. 2(b)].

We can also estimate the number $n(l_r)$ of field peaks within one resonating square of the size l_r. In the high-contrast system (with $|\epsilon_m/\epsilon_d|\gg 1$) each field maximum of the renormalized system (with $|\epsilon_m/\epsilon_d|=1$) splits into $n(l_r)$ peaks of the E_m amplitude located along a dielectric gap in the "dielectric" square of the l_r size (see Figs. 1 and 2). The gap "area" scales as the capacitance of the dielectric gap, so must do the number of field peaks in the resonance square. Therefore, we estimate that

$$n(l_r)\propto(l_r/a)^{s/\nu}. \tag{5}$$

In accordance with the above considerations, the average (over the film surface) intensity of the local field is enhanced as $G_2=\langle|E/E_0|^2\rangle\sim(E_m/E_0)^2 n(l_r)(\xi_A/\xi_e)^2\sim(a/\xi_A)^2|\epsilon_m|^{3/2}/(\epsilon_m''\epsilon_d^{1/2})$, where we used Eqs. (2), (4), and (5) and the critical exponents $t=s=\nu=4/3$; the angular brackets hereafter stand for averaging over the film. Thus, using simple arguments based on the scaling dependences of $\epsilon_m(l)$ and $\epsilon_d(l)$ on l and the resonance condition $-\epsilon_m(l_r)=\epsilon_d(l_r)$, one can define the renormalization procedure that allows one to rescale the "high-contrast" system to the renormalized one with $-\epsilon_m=\epsilon_d=1$.

The high-order moments of the local field, which define local-field enhancement for nonlinear optical processes, can be estimated as $G_n\equiv M_{k,m}=\langle|E|^k E^m\rangle/|E_0|^k E_0^m\sim(E_m/E_0)^n n(l_r)(\xi_A/\xi_e)^2$, where $n=k+m$. Using the scaling formulas (2)–(5) for the field distribution, we obtain the following estimate for the field moments $G_n\sim(E_m/E_0)^n(l_r/a)^{s/\nu}(\xi_e/\xi_A)^2$, i.e.:

$$G_n\sim\left(\frac{|\epsilon_m|^{3/2}}{(\xi_A/a)^2\epsilon_d^{1/2}\epsilon_m''}\right)^{n-1}, \tag{6}$$

for $n>1$ and $k>0$ (where, again, we took into account that for two-dimensional percolation composites, the critical exponents are given by $t\cong s\cong\nu\cong 4/3$). Note that if $k=0$ in $M_{k,m}$ (i.e., $G_n=\langle E^n/E_0\rangle$), then, because of the destructive phase interference, the enhancement is different from Eq. (6); it is discussed in detail in Refs. 11,16.

For silver-glass percolation films, for example, with $\omega_p=9.1$ eV and $\omega_\tau=0.021$ eV, we find that the average field-enhancement can be as large as $G_{RS}\sim\langle|E|^4\rangle/|E_0|^4=M_{4,0}\sim 10^7$, for Raman scattering, and as $G_{FWM}\sim\langle|E|^2 E^2\rangle/|E_0|^2 E_0^2=|M_{2,2}|^2\sim 10^{14}$, for degenerate four-wave mixing. The local field intensity in the hot spots can approach the magnitude 10^5 so that the *local* enhancement for nonlinear

optical responses can significantly exceed the average one and be truly gigantic, up to 10^{10}, for Raman scattering, and up to 10^{20}, for four-wave mixing signals. With this level of enhancement, one can perform *nonlinear* spectroscopy of single molecules and nanocrystals. It is important that the enhancement can be obtained in the huge spectral range, from the near-UV to the far-infrared, which is a big virtue for spectroscopic studies of different molecules and nanocrystals. We also note that the field enhancement provided by semicontinuous metal films can be used for various photobiological and photochemical processes.

The estimates obtained above from simple qualitative considerations are in agrement with the results of Ref. 11 following from more rigorous considerations; they are also supported by numerical simulations described in Refs. 11 and 13. Below we discuss our experimental near-field optical studies of percolation metal-dielectric films.

III. NEAR-FIELD OPTICAL MICROSCOPY AND SPECTROSCOPY OF PERCOLATION FILMS

To study the field distribution considered above we used scanning near-field optical microscopy. First we describe our apparatus and the theoretical modeling used for interpretation of the obtained SNOM images and spectra. Then we present and discuss the obtained experimental results and compare them with numerical simulations.

A. SNOM description and theoretical modeling of SNOM imaging

We imaged the localized optical excitations in gold-on-glass percolation films, using scanning near-field optical microscopy (SNOM). The used SNOM probe is an apertureless tip made of a tungsten wire etched by electrochemical erosion.[31] The radius of curvature of the tip measured by scanning electron microscopy is about 10 nm, which provides very high spatial resolution needed to image the localized optical modes. The tip oscillates above a sample which is attached to an (x,y) horizontal piezoelectric stage. The tip is the bent end of the tungsten wire used as a cantilever connected to a piezoelectric transducer that can excite it perpendicularly to the sample surface. The frequency of vibrations (~ 5 kHz) is close to the resonant frequency of the cantilever and its amplitude is about 50 nm. The tip vibrates above the sample in the tapping mode regime of the atomic force microscope (AFM). Detection of the vibration amplitude is made by a double photodiode, detecting the lever-arm shadow in a laser diode probe beam. A feedback system, including a piezoelectric translator attached to the piezoelectric transducer (needed for the tip vibrations), keeps constant the vibration amplitude during the sample scanning. The detection of the feedback voltage applied to the piezoelectric translator gives a topographical image of the surface, i.e., the AFM signal that can be taken simultaneously with the SNOM signal. A first microscope objective focuses the light of tunable Ti:sapphire laser (with pulse duration ~ 200 fs and repetition rate 76 MHz) on the bottom surface of the sample. The signal collection is axially symmetric above the
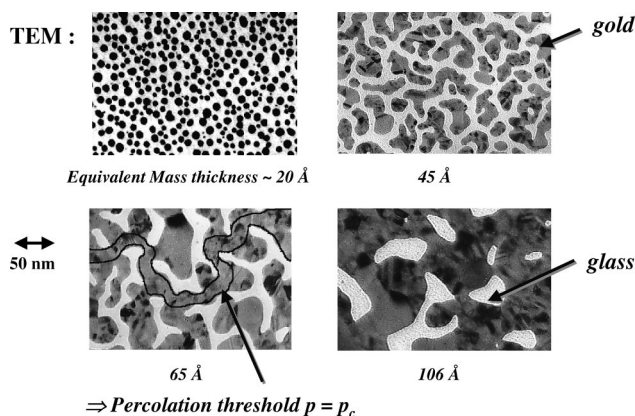

FIG. 3. TEM pictures of gold-glass films at different metal filling factors. Percolation (semicontinuous) film is formed at the effective gold-metal thickness 6.5 nm.

sample and it is made by a second microscope objective. The transmitted light passing through the microscope is then sent to a photomultiplier.

The tip vibration modulates the near-zone field on a sample surface and lock-in detection of the collected light at the tip's vibrational frequency allows one to detect the locally modulated field.[31] We note that the detected signal in such SNOM technique is proportional to the amplitude of the modulated local field rather than its intensity. In order to relate our results to other near-field measurements (where the local intensity is typically measured) the results shown below are squared to display the intensity of the detected signal.

For the visible and near-IR parts of the spectrum, the tungsten tip ($n \approx 3.5 + 2.8i$) does not have any resonances so that its polarizability is much less than the polarizability of the resonance-enhanced plasmon oscillations of the film. Because of this, perturbations in the field distribution introduced by the tip are relatively small. Our calculations of the tip perturbations, when it is modeled as a polarizable sphere, support this conclusion.[31]

Note that for our local photomodification studies we also used photon scanning tunneling microscope (PSTM) described in Sec. III D. Samples of semicontinuous gold films were prepared by depositing gold thin films on a glass substrate at room temperature under ultrahigh vacuum (10^{-9} Torr). In order to determine a closeness to the percolation threshold the resistivity and the deposited mass thickness were measured all along the film deposition. Optical reflection and transmission of the samples were also determined out of the vacuum chamber and compared with the well-known optical properties of percolation samples.[22,32] Transmission electron microscopy was performed afterwards by depositing the same film on a Cu grid covered by a very thin SiO_2 layer.

TEM pictures of glass-gold films at different filling factors are shown in Fig. 3. For our local photomodification study we also used silver semicontinuous films prepared by laser ablation as described in Sec. III D.

To process the SNOM data we used the following procedure. First, we removed a "pseudoslop" in the optical data
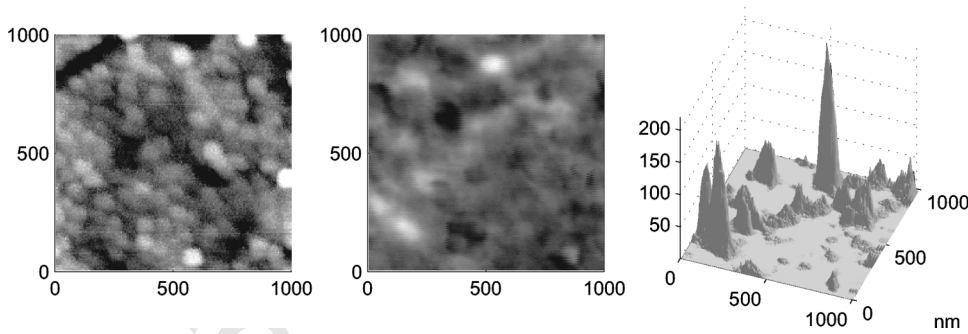
FIG. 4. Left: Typical AFM image (the height varies between 0 and 10 nm). Center: SNOM image of percolation gold-glass film ($\lambda = 780$ nm; the optical contrast is 92%). Right: Local field-intensity distribution for the same area obtained by processing the SNOM image, as described in the text.

set, resulting from imperfections in the feedback loop (which also leads to slight change in the amplitude of the tip oscillations during the scanning) and, most importantly, from a drift of the whole set up. Such drift is typical for SNOM studies and often complicates interpretation of SNOM images. The drift was also seen in our AFM pictures of the samples which were known not to have any slop. To remove this pseudoslop in the SNOM data, we first averaged the data for a number of cross sections along the "x" and "y" axes and then, using the least-square fit, we defined the average slops in the x and y directions; these two average slops in turn allowed us to define the coordinates of the plane of inclination. To reveal the actual field distribution, this plane was brought back to the $z=0$ plane. The noise below zero appearing as a result of the used procedure was removed, which statistically does not affect the field distribution.

Then, as mentioned, we squared the detected signal in order to find the local field intensity. To find the local enhancement we normalized the local intensity by the mean of the detected signal squared that represents the intensity of the applied field. This is because the average local field on a percolation film, as shown in Ref. 11, is simply equal to the applied field, $\langle E \rangle = E_0$, so that when squared it gives the intensity of the applied field $I = E_0^2$.

The left-hand-side picture in Fig. 4 shows typical AFM image (with the height varying between 0 and 10 nm) and the central picture shows a "raw" SNOM image of the same section of a percolation gold-glass film. The local field-intensity distribution found by processing the SNOM image, in accordance with the procedure described above, is shown in the right-hand-side picture in Fig. 4. The SNOM image was obtained at $\lambda = 780$ nm and linear polarization of incident light; the optical contrast for the SNOM image in Fig. 4 is 92%. For control, in all our SNOM experiments described below we have also taken AFM pictures. However, we omit, for simplicity, these AFM images, for which the one in Fig. 4 is a typical representative.

We also performed a theoretical modeling for SNOM imaging. To do the modeling, we first found that the local SNOM signal at the tip's height of 20 nm is approximately equal to the average signal detected by SNOM in the tapping, i.e., oscillating mode [for accuracy, we averaged our calculations over many different (x,y) spatial positions]. The detected signal in our SNOM is, in fact, averaged over all the heights between 0 to 100 nm (or what is the same, over the period of the tip's vibrations). In our modeling, we calculated a signal at the fixed "effective" height of 20 nm that roughly approximates the height-averaged signal of the SNOM. In addition, to simulate the finite-size effect for the tip, the data at the effective height of 20 nm were averaged over the circular area of the radius 10 nm (representing the size of our tip), with the Gaussian weight function within the circle. The numerical method used to calculate the local fields on percolation films is based on real-space renormalization group and it is described in detail in our previous papers.[11–13]

B. Imaging and spectroscopy of plasmon modes

Using our SNOM we imaged localized optical excitations and studied their local near-field spectra. In Fig. 5, we show experimental (a) and calculated (b) near-field images on the surface of a percolation gold-glass film, for different wavelengths, $\lambda = 720$ nm and $\lambda = 790$ nm. It needs to be said here that experimental and simulated samples are, on average, similar but, indeed, different locally. (Note also that because of photocathode's different sensitivity at 720 and 790 nm, the detected local intensity at 790 nm should be multiplied by roughly a factor of 10.) As mentioned, AFM pictures were always taken along with SNOM images, to control the imaging. In experimental SNOM images, resolution of one pixel is 16 nm, which is near the best resolution that can be achieved by SNOM. Our SNOM allows one to resolve even the most localized modes, with the localization radius of an order of 10 nm, i.e., about two orders of magnitude smaller than the optical wavelength.

One can see that, in accordance with theoretical predictions, there are sharp peaks representing the hot spots in the field distribution. We also note that although the detected field enhancement is of the order of 10^2 to 10^3, the actual enhancement right on the film surface (experienced, for example, by molecules adsorbed on the surface) is much stronger, and can reach the values between 10^4 and 10^5, as shown in Ref. 13. The decrease in the observed enhancement occurs because, as mentioned, the signal detected by the SNOM oscillating tip is averaged over all tip-surface separations, from 0 nm, where the enhancement is the largest, to 100 nm, where the enhancement is negligible. We also note that in agreement with theoretical predictions most localized hot spots can be as small as 10 nm only.

In Fig. 6 we show detected SNOM images (a) and theoretical calculations (b) for two different linear s polarizations, perpendicular to each other, at the same wavelength $\lambda = 780$ nm. (Note that the local intensities in Fig. 6(a) should be multiplied by roughly a factor of 6 as a result of
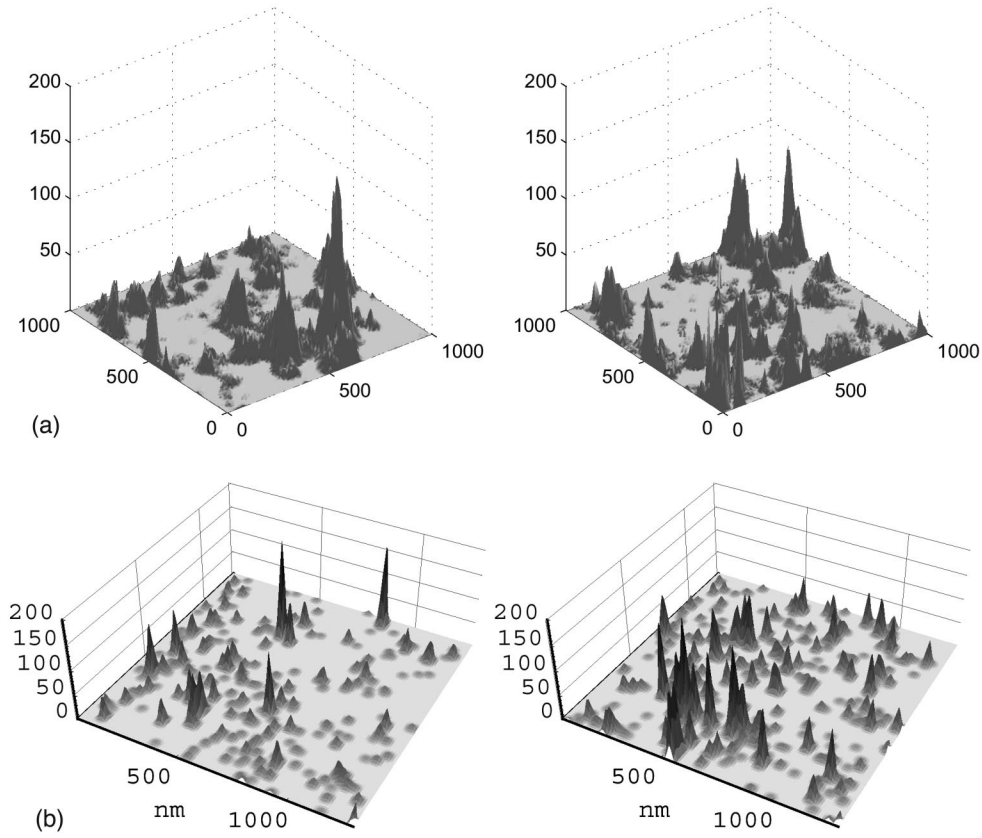
FIG. 5. Experimental (a) and calculated (b) SNOM images of localized optical excitations in percolation gold-glass film for different wavelengths $\lambda = 720$ nm and $\lambda = 790$ nm.

renormalization of detector's sensitivity for 780 nm.] As one can see the field distribution differs significantly for the two different s polarizations. Similar strong changes in the hot spot positions also occur at transition from the s to p polarization (not shown). The strong polarization dependence observed indicates the anisotropic character of plasmon modes on a semicontinuous metal film.

Thus, we see that the spatial position of hot spots changes with both, light polarization and wavelength. As our experiments and calculations show the field distribution changes significantly, even at very small change of the wavelength, such as 10 nm.

In accordance with theoretical considerations of Sec. II, for percolation films, the renormalized elements formed by dielectric and metallic clusters (rather than individual particles) resonate in the near infrared and provide the largest field peaks. These peaks are much larger than those obtained at the frequency corresponding to the resonance of individual particles. According to Eq. (3), at the transition from the visible, with $|\epsilon_m| \sim \epsilon_d$ (i.e., $\omega \sim \tilde{\omega}_p$), to the near infrared, with $|\epsilon_m| \gg \epsilon_d$ (and $\tilde{\omega}_p \gg \omega \gg \omega_\tau$), the local fields increase in the amplitude and saturate at the magnitude given by $E_m/E_0 \sim \epsilon_d^{-1/2}(a/\xi_A)^2(\omega_p/\omega_\tau)$.

To verify this we also imaged the field distribution for the visible spectral range, at 514 nm (which is close to the resonance of individual gold particles) and compared it with the

fields in the near-infrared. By checking the fields in Fig. 7 against those in Figs. 4–6, we conclude that the field peaks become significantly larger at the transition from the visible (Fig. 7) to the near infrared (Figs. 4–6), in agreement with theoretical predictions.

To summarize this part, we note that in agreement with theoretical calculations our SNOM studies show that the optical excitations on metal-dielectric films are localized, so that the smallest hot spots can be as small as 10 nm in size. The positions of the hot spots associated with the localized plasmon oscillations exhibit a very strong sensitivity to both wavelength and polarization of an incident beam. Local field peaks in the hot spots increase from the visible toward the infrared.

We also performed the near-field spectroscopy of percolation films, by parking an SNOM tip at different points of the surface and varying the wavelength. This nanospectroscopy allows one to determine the local resonances of nm-size areas right underneath the tip; the nanostructures at different points resonate at different λ independently leading to different local near-field spectra. The spectra characterize λ dependence of the field hot spots associated with the localized plasmon modes.

In Fig. 8 we show the measured (a) and calculated (b) near-field spectra taken at different points of the film. There is qualitative agreement between theory and experiment. The
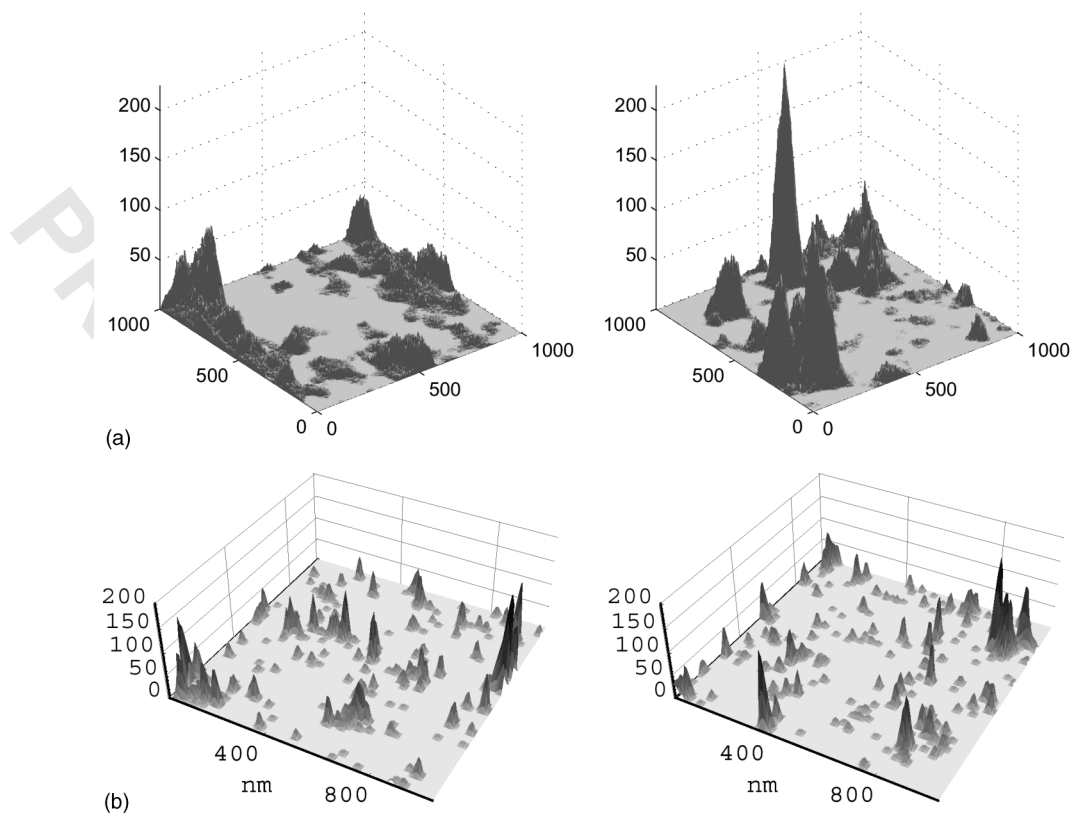
FIG. 6. Experimental (a) and calculated (b) SNOM images of field distribution in percolation gold-glass film for two different linear *s*-polarizations (perpendicular each other) of an incident light at $\lambda = 780$ nm.

spectra are similar to those obtained previously in Ref. 10 and consist of several peaks ~ 10 nm in width. The spectra depend markedly on spatial location of the point where the near-field tip is parked. Even as small shift in space as 50 nm results in different spectra, which is a strong evidence of the plasmon localization. We note that for continuous metal (or dielectric) films neither sub-λ hot spots nor their local spectra can be observed, because, in this case, optical excitations are delocalized and homogeneous. Below we consider a novel effect observed in semicontinuous metal films, giant local optical activity.
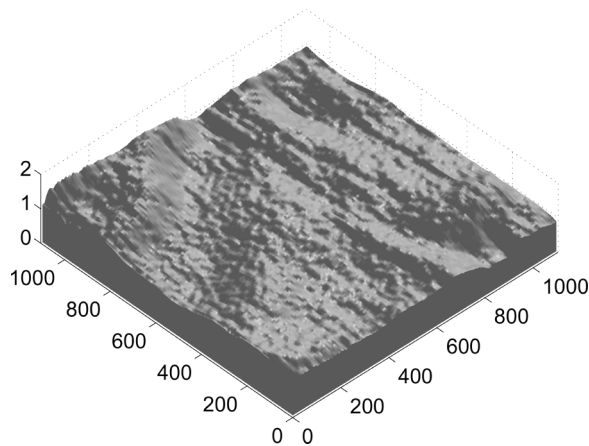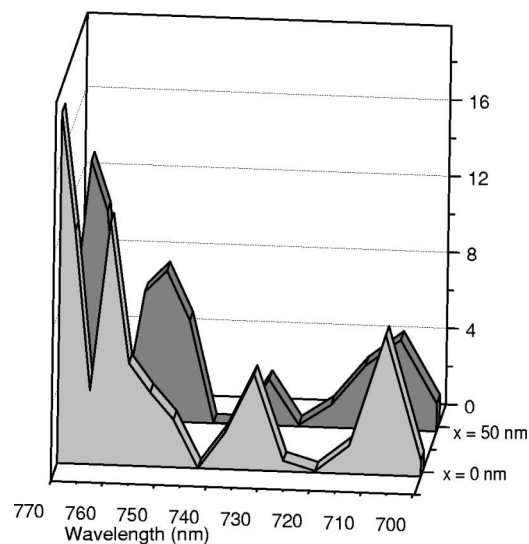

FIG. 7. SNOM image of optical excitations of semicontinuous gold film at $\lambda = 514$ nm.
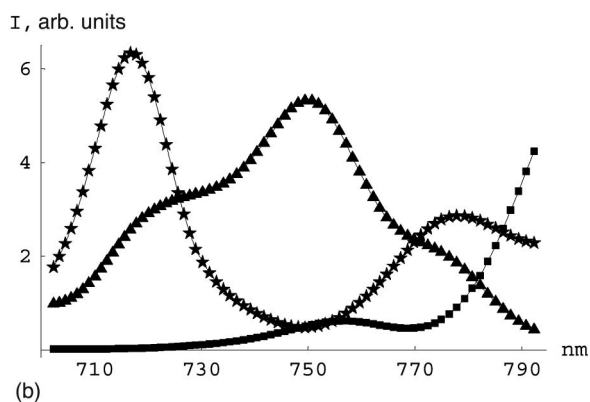
C. Local optical activity

Typically, optical activity is observed for macroscopically large objects with unbalanced amount of left and right handed molecules. This effect, in particular, can be used to distinguish the enantiomers from each other, which is very important because the physiological and pharmacological effects of the enantiomers can be very different.[33]

It was recently shown that a giant *local* optical activity can occur in fractal aggregates of colloidal particles.[34,35] One can anticipate that similar effect may occur in a percolation film, which can be thought of as a collection of fractal clusters of different sizes, from very small ones up to the "infinite" percolation cluster. There is still an important difference: a percolation film is homogeneous on a macroscopic scale, whereas an ideal fractal is inhomogeneous in all scales. Really, because of self-similarity of fractals, there are voids that are present in all sizes, from the size of a single particle to the size of the whole cluster. In both objects, however, there is localization of optical excitations within small, nm-sized structures, which can be chiral active and thus lead to *local* optical activity. In our considerations of local optical activity in semicontinious metal films we used similar approaches as in Ref. 35.

Optical activity phenomena exhibit differences in attenuation (circular dichroism), refraction (circular birefringence), and scattering for right- and left-circularly polarized light. The scattering optical activity is denoted as circular intensity differential scattering (CIDS).[36−38]
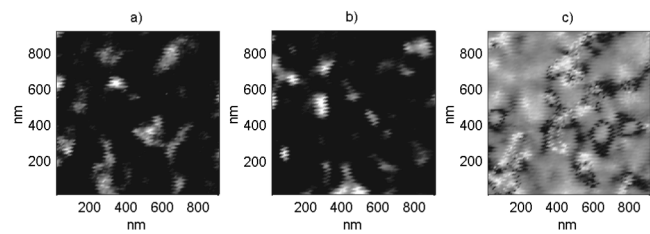
FIG. 9. SNOM images of gold-glass percolation films with (a) right- and (b) left-circularly polarized incident light at 780 nm. (c) Local CIDS signal computed from the two images shown in (a) and (b). Raw data is shown.

FIG. 8. Experimental (a) and calculated (b) near-field spectra at different spatial locations (50 nm apart) of the film. (Arbitrary intensity units are used.)

The described above linear polarization dependence, in particular, illustrates strong local anisotropy of plasmon modes in percolation films. However, an important question, whether the plasmon modes exhibit handedness still needs to be addressed. It is known, for example, that two coupled anisotropic oscillators lying in different planes represent a simple model of a chiral system. Semicontinuous metal films are formed by chains of particles with almost all possible local configurations. These local structures have typically neither center nor plane of symmetry and thus may have handedness so that a plasmon mode, provided that it is localized on such a structure, exhibits chirality. However, macroscopic effects are significantly reduced for a racemic mixing of chiral elements (approximately equal amounts of elements with opposite handedness). Therefore, the local optical activity detected using SNOM may be much stronger than typically observed macroscopic effects and it provides important information on chirality of local structures and their statistical properties.

Metal particles forming percolation films are typically 10 nm in size and the local resonating structures, ''hot'' spots, vary in size between tens to hundreds nanometers, i.e., can

be comparable with the light wave length. It is also important that a typical thickness of a semicontinuous metal film, ~ 10 nm, is comparable to the skin depth, so that the field changes significantly in the vertical direction. Therefore, the optical activity, which is a nonlocal propagation effect and requires spatial dispersion, can be large for chiral elements of a semicontinuous metal film. Moreover, since plasmon modes are characterized by large resonance quality factors the optical activity effect can experience the resonant enhancement.

Figures 9(a) and 9(b) show the local SNOM images of a percolation film for right- and left-circularly polarized incident light, respectively. Both images exhibit large variations of light intensity and many hot spots. Visual examination of the two images reveals different spatial distributions of hot spots for the two opposite circular polarizations, indicating circular differential response in certain regions. The weak correlation of the two images is confirmed by a correlation analysis as illustrated in Fig. 10, where the cross-correlation function $g_c(\mathbf{R}) = C_1[\langle I_L(\mathbf{r}) I_R(\mathbf{r}+\mathbf{R}) \rangle - \langle I_L(\mathbf{r}) \rangle \langle I_R(\mathbf{r}) \rangle]$ and autocorrelation function $g_{ac}(\mathbf{R}) = C_2[\langle I_{L,R}(\mathbf{r}) I_{L,R}(\mathbf{r}+\mathbf{R}) \rangle - \langle I_{L,R}(\mathbf{r}) \rangle^2]$ for the two images are shown [the normalization constants C_1 and C_2 are chosen so that $g_{ac}(0)=1$ and, if the intensities of scattered light had been equal for the two circular polarization inputs, $g_c(0)=1$]. The autocorrelation functions for the right- and left-circularly polarizations (stars and triangles in Fig. 10, respectively) are essentially the same, indicating that, *on average*, the field distributions are almost identical for the two circular polarizations. The autocorrelation functions are, however, very different from the cross-correlation function of the two images (boxes in Fig.
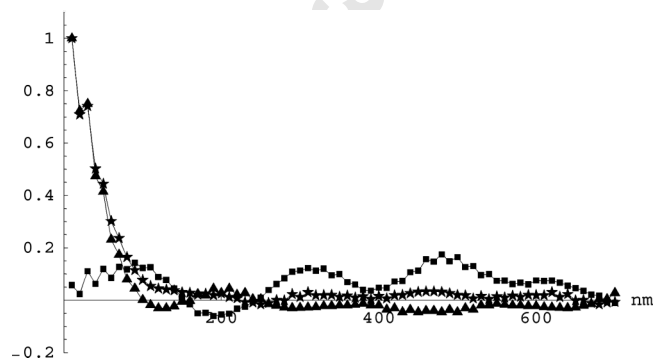

FIG. 10. Cross-correlation and autocorrelation functions computed from the two images shown in Figs. 9(a) and 9(b).
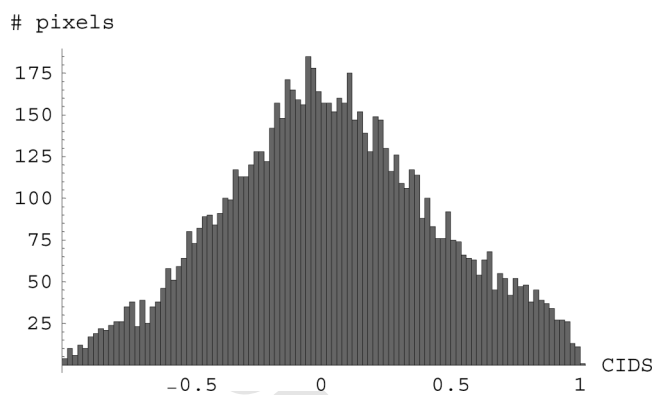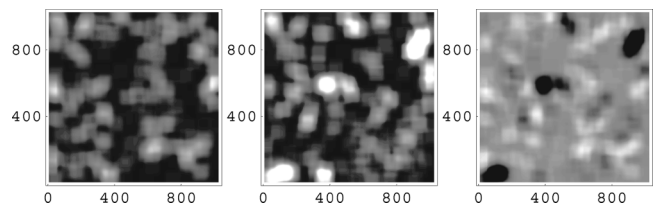
FIG. 11. Histogram for local CIDS parameter.

FIG. 12. Numerical simulations for local field distribution (arbitrary units) for model percolation gold-glass film for right (left-hand side), left (center) circular polarizations of incident light ($\lambda = 780$ nm), and local CIDS signal (right-hand side).

10), which is close to zero even at small distances R, indicating nearly no correlation in the intensity distributions for the two circular polarizations. Our control SNOM measurements on a continuous gold film reveal no hot spots, showing instead a uniform field distribution with no observable enhancement.

The scattered intensities for right- and left-circularly polarized incident light can be related to elements of the Mueller scattering matrix $S_{\alpha\beta}$ as $I_{R,L} = I_0(S_{11} \pm S_{14})$, where S_{11} gives the total scattered intensity and S_{14} characterizes optical activity.[39] In terms of the Mueller elements, the scattered intensities for right- and left-circularly polarized incident light are given by $I_{R,L} = I_0(S_{11} \pm S_{14})$. The dimensionless parameter that describes circular intensity difference scattering is $S_{14}/S_{11} = (I_R - I_L)/(I_R + I_L)$.[36,39]

Figure 9(c) shows distribution for the local CIDS parameter $(I_R - I_L)/(I_R + I_L)$ computed from the optical images shown in Figs. 9(a) and 9(b). The white and black spots in Fig. 9(c) represent areas of preferential scattering for right- and left-circularly polarized incident light, respectively. The variations in the parameter CIDS demonstrate that a semicontinuous metal film is characterized by a broad and random distribution of chiral elements associated with the plasmon modes.

The randomness in distribution of plasmon modes with different handedness is characterized by a histogram for the number of pixels sorted in accordance with the CIDS sign and value, as shown in Fig. 11. The distribution is broad, with the half width at the half maximum being about 0.5. Despite weak asymmetry, the histogram shows approximately equal numbers of chiral areas with opposite handedness.

The local optical activity observed is large ($|(I_R - I_L)/(I_R + I_L)| \sim 1$) and varies strongly with wavelength. The sign of $(I_R - I_L)/(I_R + I_L)$ can change, even for very small changes of wavelength, ~ 10 nm. In sharp contrast, the value of the CIDS parameter averaged over the whole 0.9×0.9 μm^2 sample, is much smaller: $|(I_R - I_L)/(I_R + I_L)| = 0.036 \pm 0.004$. The macroscopic absorption spectra of our samples have a flat wavelength dependence in this spectral range, with no spectral structures. This is in sharp contrast with the local spectra taken for different circular polarizations.

All these results clearly show that, while locally there exist areas of strong preference for scattering of one circular polarization or the other, this preference is effectively absent when averaged over a macroscopic sample. This result opens new avenues in optical activity studies where *local* gyrotropy effects may be investigated using near-field optical microscopy.

We also simulated the observed effect of local optical activity. In our simulations we used the approach based on the discrete dipole approximation (DDA) and replaced the metallic component of a semicontinuous metal film by array of dipoles representing metallic spheres with the radius $R_m = (3/4\pi)^{1/3}a$, where a is the lattice period. Such geometrically intersecting spheres have the same total volume as the volume of the metal component and effectively take into account multipolar corrections (for details, see Ref. 16). To simulate the finite thickness of the film we generated two different metal-dielectric percolation layers and placed them on top of each other, so that the thickness of the film was 10 nm as in experiments. Then we numerically solved the coupled dipole equations (CDE's), with the interaction represented by the full Green's function, including the near-, intermediate-, and far-field terms ($\propto r^{-3}$, r^{-2}, and r^{-1}, respectively; for details of such numerical approach see Ref. 16). Such approach allows one to take into account the spatial dispersion effects important for optical activity.

Results of our simulations for the local-field distribution induced by left and right circularly polarized light are shown in Fig. 12. In agreement with experimental observations, our simulations also show strong local optical activity expressed in different locations of hot spots for the two circular polarizations of incident light.

Thus, percolation metal-dielectric films manifest giant *local* optical activity. The effect occurs because the plasmon modes on a semicontinuous metal films are not only anisotropic but also may have handedness.

D. Local photomodification

In this section we discuss our studies on local photomodifications. The samples of semicontinuous metal films used for the photomodification studies were prepared by the laser ablation technique. A silver target was placed in a vacuum chamber with base pressure of 1 mTorr. After pumping for 24 h, the vacuum chamber, when sealed, had an outgas/leak rate lower than 2 mTorr/h. Prior to a laser ablation run, the chamber was filled with argon to ~ 10 Torr. A Nd:YAG la-

Local Photomodification of a Silver Percolation Film

Before Irradiation
(image beam: cw, 633 nm)   **After Irradiation**
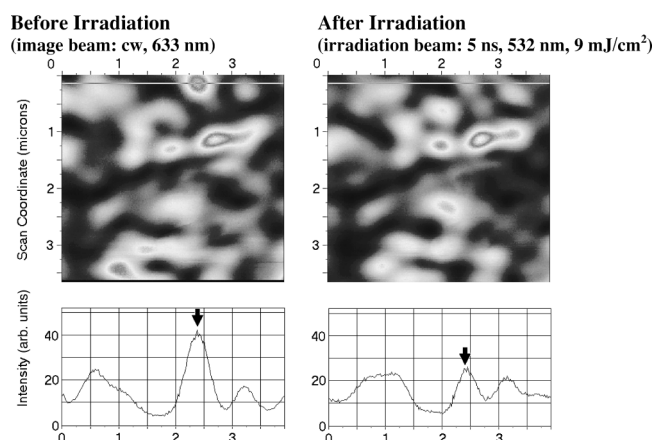(irradiation beam: 5 ns, 532 nm, 9 mJ/cm^2)

FIG. 13. PSTM images of seminontinuous silver film before and after photomodification of the sample using nanosecond laser pulses at 532 nm. The PSTM images were recorded using the probe wavelength at 633 nm.

ser (Quanta-Ray DCR) was used as the laser ablation source. The laser provided 0.2-J, 8-ns, 1064-nm pulses at a 10-Hz repetition rate. The laser beam was focussed onto the target and the beam diameter at the target surface was 1.5 mm. The ablated silver material was deposited onto a glass substrate and a carbon-coated TEM sample grid, both placed a few centimeters in front of the target. A 125-keV Hitachi H7000 electron microscopy was used for the TEM studies. According to TEM images (not shown) the samples prepared by the laser ablation technique have similar structure as the films made by thermal evaporation in a vacuum chamber and used for studies described in the preceding sections.

The thin films deposited on glass substrates were investigated using photon scanning tunneling microscope (PSTM) modified from a commercial atomic force microscope (Quesant Q250). The samples were mounted to the hypotenuse face of a right-angle prism with an index matching fluid. A sample was illuminated by the evanescent field in the total internal reflection geometry and the local optical signal was collected through an uncoated optical fiber. Two helium-neon lasers, one operated at wavelength of 543 nm and the other at 633 nm, were used as the illumination source. The probe laser beam was s polarized at the sample surface. The optical fiber was sharpened to approximately 50 nm in radius at the tip using a fiber puller (Sutter Instruments P-2000). The separation between the fiber tip and a sample was regulated using non-optical shear-force feedback.

The photomodification was achieved by irradiating the sample using ten 5-ns pulses of the second harmonic output of a Nd:YAG laser (Quantel Brilliant) at 532 nm. The modification laser beam was incident from above at an incident angle of 70° from the surface normal and had the same polarization as the probe beam. The fiber tip was retracted during pulsed-laser irradiation. The retraction of the tip avoided possible damage of the tip by the nanosecond pulses and possible perturbation of the optical field by the tip.

Figure 13 shows near-field optical images of a semicon-

tinuous metal film at probe laser wavelength λ_{probe} $= 633$ nm. The PSTM images show a very inhomogeneous distribution of optical intensity. The minimum feature size is 200 nm, corresponding to the lateral resolution of our PSTM. The theoretical minimum feature size is smaller by an order of magnitude.

The image shown in Fig. 13(b) was recorded at the same area of the sample imaged in Fig. 13(a), but after irradiation by 10 nanosecond laser pulses. The incident laser energy density was 4.5 mJ/cm^2. The two images in Fig. 13 share many common features. There are, however, large differences at a few locations. The high-intensity area (i.e., hot spot) at $x = 2.4$ μm and $y = 0.1$ μm, which existed before irradiation, substantially decreases its intensity after irradiation. The intensity plots along the indicated horizontal line shows that the optical intensity is reduced by 40% at this location. Although not shown in Fig. 13, nanosecond laser irradiation can also create new hot spots.

The modification of the optical intensity distribution exhibits a threshold nature. The threshold is observed to be ~ 10 mJ/cm^2 per pulse. Qualitatively the same results have been observed at $\lambda_{probe} = 543$ nm.

To simulate the photomodification, the local field distribution at wavelength of 532 nm is calculated. To simplify the calculation, the incident wave is assumed to propagate along the surface normal direction. Since we are interested in a qualitative comparison of the calculated and experimental results, the different incident angle used in the calculation (0°) from that in the experiment (70°) should be of minimum effects. After the local field distribution at $\lambda = 532$ nm is calculated the film is modified by "eliminating" conducting particles located at the sites where the local fields were greater than a threshold value. Such simple model assumes that the particles experiencing the photomodification do not contribute any more to the resonant excitation.[40] The threshold value is chosen to keep the number of the eliminated particles to be 1% of the total particles.

Our calculations show that at the pump power used in our experiments the local temperature increase in the hot spots is up to about half of the melting temperature (see also Ref. 40). Zhu and Averback have demonstrated by molecular dynamic simulations that metal nanoparticles that are in contact with each other and heated to about 1/2 of the melting temperature do not behave as rigid bodies.[41] In particular, the local shear stress near the necks (touching points) was shown to be large enough to cause plastic deformation and eventual sintering of the nanoparticles. There is experimental evidence to support their conclusion.[42] Although the exact mechanism of the photomodification is not completely understood at the present time, it seems very plausible that photomodification is caused by such sintering.

The local field distribution functions were calculated before and after the photomodification. The results are shown in Figs. 14 and 15 for two probe wavelengths at λ_{probe} $= 543$ and 633 nm, respectively. The same wavelengths were used in the experiment. Both Figs. 14 and 15 show the effect of local photomodification (disappearance of some of the hot spots and appearance of some new ones) after irradiation with the pump at $\lambda = 532$ nm above the modification thresh-
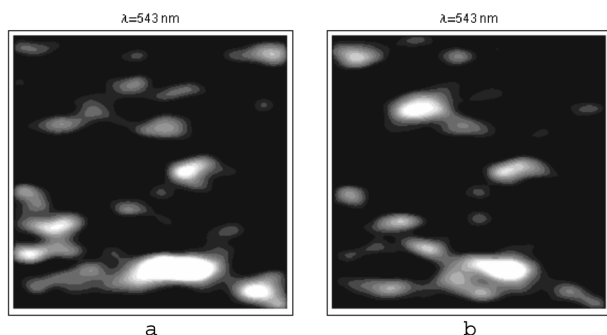
FIG. 14. Theoretical simulation of near-field optical signal at probe wavelength $\lambda_{probe} = 543$ nm for a semicontinuous silver film (a) before and (b) after modification, induced by the pump at $\lambda = 532$ nm. The length scales are in units of micrometer.

old. The effect of photomodification can be observed at the same as (or close to) the pump wavelength and at significantly different wavelengths. The field distribution was calculated at ~ 10 nm distance above the surface using the dipole approximation. The data were then averaged over an area of 50 nm. Thus, theoretical results plotted in Figs. 14 and 15 have taken into consideration the finite sample-tip distance and finite aperture size in the experiment.

Let us consider first Fig. 14. The pair of calculated images at the same probe wavelength of $\lambda_{probe} = 543$ nm before and after the modification is quite different. Previously existed hot spots (e.g., at $x = 2.5$ μm, $y = 2.4$ μm, and at $x = 2.3$ μm, $y = 0.2$ μm) lost their intensity substantially after the modification. New hot spots are created after the modification (e.g., at $x = 0.8$ μm, $y = 1.9$ μm). However, the two images still share some common features. The very large hot spot around $x = 1.5$ μm, $y = 0.4$ μm, for example, appear at both images although their shapes are somewhat different. Similarly, the pair of calculated images at $\lambda_{probe} = 663$ nm before and after the modification (Fig. 15) exhibits different features but also somewhat correlated. These theoretical results are in qualitative agreement with the experimental data. It appears that there are more changes in theoretical results than in the experimental data. This is because the experiments were performed with the photomodification laser beam at a power just slightly above the threshold. A much greater changes were observed experimentally if the laser power was doubled.

The following picture for the photomodification process emerges from our experimental and theoretical studies: During nanosecond-laser irradiation of a semicontinuous metal film, the laser energy is not uniformly distributed over the sample surface. Rather, it is localized at hot spots, where, provided that the pump exceeds the photomodification threshold, the sintering of particles occurs. Such geometric changes in turn result in modification of local optical intensity. Some previously existing hot spots are diminished after irradiation and new hot spots are created when probed at wavelengths either close to or different from the irradiation laser wavelength. The local contrast changes (by factors of up to $\sim 100\%$) are much greater than the spectral "hole" in the macroscopic absorption measured in the far field, which is about $\sim 1\%$.
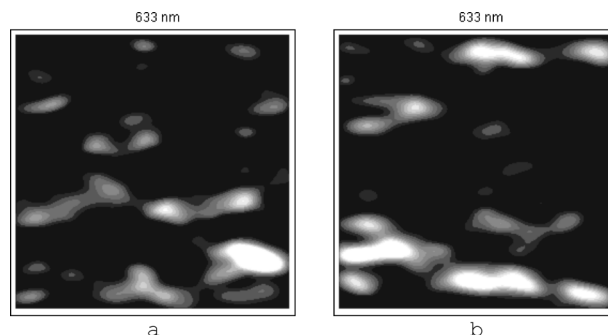

FIG. 15. The same as Fig. 14 except $\lambda_{probe} = 633$ nm.

IV. CONCLUDING SUMMARY

The near-field optical studies described in this paper support main conclusions of the recently developed theory[11,17] and can be summarized as follows. (i) The optical excitations in metal-dielectric films near the percolation threshold experience localization so that the electromagnetic energy is concentrated in small nanometer-size areas, hot spots, where the plasmon modes are localized. (ii) The hot spot spatial positions are strong functions of the wavelength. (iii) The plasmon modes are anisotropic and, therefore, there spatial positions depend on the incident light polarization. (iv) The local field intensity in the hot spots exceeds the intensity of the incident light by several orders of magnitude and it dramatically increases at transition from the visible to the infrared. Because of localization, different areas, with different geometries, resonate independently at different frequencies. In accord with this, (v) the local near-field spectra of plasmon modes, consisting of several peaks with widths ~ 10 nm, are very different for different spots, even if they are only ~ 50 nm apart. (vi) The localized plasmon modes on a semicontinuous film may possess handedness and thus they show the effect of strong local optical activity. In accordance with this, the hot spot distributions observed by SNOM with the right- and left-circularly polarized incident light are very different; however, the effect occurs only *locally*; on average, the film does not show the macroscopic optical activity. Finally, (vii) provided that the pump power exceeds the threshold ~ 10 mJ/cm^2, it can induce local photomodification in the hot spot areas. This photomodification probably occurs due to sintering of particles in the hot spots. All the observations summarized above support basic predictions of theory[11,17] and they are in good accord with accompanying numerical simulations.

[1] J. E. Sipe and R. W. Boyd, Phys. Rev. B **46**, 1614 (1992); R. J. Gehr, G. L. Fisher, R. W. Boyd, and J. E. Sipe, Phys. Rev. A **53**, 2792 (1996); G. L. Fisher, R. W. Boyd, R. J. Gehr, S. A. Jenekhe, J. A. Osaheni, J. E. Sipe, and L. A. Weller-Brophy, Phys. Rev. Lett. **74**, 1871 (1995); R. W. Boyd, R. J. Gehr, G. L. Fisher, and J. E. Sipe, Pure Appl. Opt. **5**, 505 (1996).

[2] D. J. Bergman and D. Stroud, in *Solid State Physics* (Academic, New York, 1992), Vol. 46, p. 147.

[3] C. Flytzanis, Prog. Opt. **29**, 2539 (1992); D. Ricard, Ph. Roussignol, and C. Flytzanis, Opt. Lett. **10**, 511 (1985); F. Hache, D. Ricard, C. Flytzanis, and U. Kreibig, Appl. Phys. A: Solids Surf. **47**, 347 (1988).

[4] H. B. Liao, R. F. Fiao, J. S. Fu, P. Yu, G. K. L. Wong, and P. Sheng, Appl. Phys. Lett. **70**, 1 (1997); K. P. Yuen, M. F. Law, K. W. Yu, and P. Sheng, Phys. Rev. E **56**, R1322 (1997); H. B. Liao, R. F. Xiao, J. S. Fu, H. Wang, K. S. Wong, and G. K. L. Wong, Opt. Lett. **23**, 388 (1988); H. B. Liao, R. F. Xiao, H. Wang, K. S. Wong, and G. K. L. Wong, Appl. Phys. Lett. **72**, 1817 (1998); W. M. V. Wan, H. C. Lee, P. M. Hui, and K. W. Yu, Phys. Rev. B **54**, 3946 (1996); D. Stroud and P. M. Hui, *ibid.* **37**, 8719 (1988).

[5] U. Kreibig and M. Vollmer, *Optical Properties of Metal Clusters* (Springer-Verlag, Berlin, 1995).

[6] *Electron Transport and Optical Properties of Inhomogeneous Media*, edited by J. C. Garland and D. B. Tanner (AIP, New York, 1978); *Electron Transport and Optical Properties of Inhomogeneous Media (ETOPIM 3)*, edited by W. L. Mochan and R. G. Barrera (North-Holland, Amsterdam, 1994); *Proceedings of the Fourth International Conference on Electrical Transport and Optical Properties of Inhomogeneous Media (ETOPIM 4)*, edited by A. M. Dykhne, A. N. Lagarkov, and A. K. Sarychev, [Physica A **241**, 1 (1997)].

[7] R. Fuchs and F. Claro, Phys. Rev. B **39**, 3875 (1989); K. Ghosh and R. Fuchs, *ibid.* **44**, 7330 (1991); F. Claro and R. Fuchs, *ibid.* **44**, 4109 (1991).

[8] G. Milton, J. Appl. Phys. **52**, 5286 (1981); D. Stroud, G. W. Milton, and B. R. De, Phys. Rev. B **34**, 5145 (1986).

[9] V. M. Shalaev, Phys. Rep. **272**, 61 (1996).

[10] S. Grésillon, L. Aigouy, A. C. Boccara, J. C. Rivoal, C. Desmarest, P. Gadenne, V. A. Shubin, A. K. Sarychev, and V. M. Shalaev, Phys. Rev. Lett. **82**, 4520 (1999).

[11] A. K. Sarychev, V. A. Shubin, and V. M. Shalaev, Phys. Rev. B **60**, 16 389 (1999).

[12] F. Brouers, S. Blacher, A. N. Lagarkov, A. K. Sarychev, P. Gadenne, and V. M. Shalaev, Phys. Rev. B **55**, 13 234 (1997).

[13] V. M. Shalaev and A. K. Sarychev, Phys. Rev. B **57**, 13 265 (1998).

[14] A. K. Sarychev and V. M. Shalaev, Physica A **266**, 115 (1999).

[15] A. K. Sarychev, V. A. Shubin, and V. M. Shalaev, Phys. Rev. E **59**, 7239 (1999).

[16] V. M. Shalaev, *Nonlinear Optics Of Random Media: Fractal Composites and Metal-Dielectric Films* (Springer Verlag, Berlin, 2000).

[17] A. K. Sarychev and V. M. Shalaev, Phys. Rep. **335**, 275 (2000).

[18] D. Stauffer and A. Aharony, *Introduction to Percolation Theory*, 2 ed. (Taylor and Francis, Philadelphia, 1991).

[19] J. P. Clerc, G. Girard, J. M. Laugier, and J. M. Luck, Adv. Phys. **39**, 191 (1990).

[20] R. W. Cohen, G. D. Cody, M. D. Coutts, and B. Abeles, Phys. Rev. B **8**, 3689 (1973).

[21] G. A. Niklasson and C. G. Granqvist, J. Appl. Phys. **55**, 3382 (1984).

[22] Y. Yagil, P. Gadenne, C. Julien, and G. Deutscher, Phys. Rev. B **46**, 2503 (1992).

[23] T. W. Noh, P. H. Song, Sung-Il Lee, D. C. Harris, J. R. Gaines, and J. C. Garland, Phys. Rev. B **46**, 4212 (1992).

[24] P. Gadenne, A. Beghadi, and J. Lafait, Opt. Commun. **65**, 17 (1988).

[25] Y. Yagil, M. Yosefin, D. J. Bergman, G. Deutscher, and P. Gadenne, Phys. Rev. B **43**, 11 342 (1991).

[26] F. Brouers, J. P. Clerc, and G. Giraud, Phys. Rev. B **44**, 5299 (1991); F. Brouers, J. M. Jolet, G. Giraud, J. M. Laugier, and Z. A. Randriamanantany, Physica A **207**, 100 (1994).

[27] D. P. Tsai, J. Kovacs, Z. Wang, M. Moskovits, V. M. Shalaev, J. Suh, and R. Botet, Phys. Rev. Lett. **72**, 4149 (1994); V. M. Shalaev and M. Moskovits, *ibid.* **75**, 2451 (1995); P. Zhang, T. L. Haslett, C. Douketis, and M. Moskovits, Phys. Rev. B **57**, 15 513 (1998).

[28] S. I. Bozhevolnyi, V. A. Markel, V. Coello, W. Kim, and V. M. Shalaev, Phys. Rev. B **58**, 11 441 (1998).

[29] S. I. Bozhevolnyi, I. I. Smolyaninov, and A. V. Zayts, Phys. Rev. B **51**, 17 916 (1995); I. I. Smolyaninov, A. V. Zayats, C. C. Davis, Phys. Rev. B **56**, 9290 (1997); I. I. Smolayninov, D. L. Mazzoni, and C. C. Davis, Phys. Rev. Lett. **77**, 3877 (1996).

[30] B. Kramer and A. MacKinnon, Rep. Prog. Phys. **56**, 1469 (1993).

[31] R. Bachelot *et al.*, Appl. Opt. **36**, 2160 (1997); P. Gleyzes *et al.*, Appl. Phys. Lett. **58**, 2989 (1991); A. Lahrech *et al.*, Opt. Lett. **21**, 1315 (1996).

[32] P. Gadenne *et al.*, J. Appl. Phys. **66**, 3019 (1989).

[33] M. Kauranen *et al.*, J. Mod. Opt. **45**, 403 (1998).

[34] S. Ducourtieux, S. Gresillon, A. C. Boccara, J. C. Rivoal, X. Quelin, P. Gadenne, V. P. Drachev, W. D. Bragg, V. P. Safonov, V. A. Podolskiy, Z. C. Ying, R. L. Armstrong, and V. M. Shalaev, J. Nonlinear Opt. Phys. Mater. **9**, 105 (2000).

[35] V. P. Drachev, W. D. Bragg, V. A. Podolskiy, V. P. Safonov, W. T. Kim, Z. C. Ying, R. L. Armstrong, and V. M. Shalaev (unpublished).

[36] L. D. Barron, *Molecular Light Scattering and Optical Activity* (Cambridge University Press, Cambridge, 1982).

[37] D. Keller *et al.*, Biopolymers **24**, 783 (1985).

[38] S. B. Singham *et al.*, J. Chem. Phys. **85**, 763 (1986).

[39] C. Bohren, D. Huffman, *Absorption and Scattering of Light by Small Particles* (Wiley, New York, 1983).

[40] V. P. Safonov, V. M. Shalaev, V. A. Markel, Yu. E. Danilova, N. N. Lepeshkin, W. Kim, S. G. Rautian, and R. L. Armstrong, Phys. Rev. Lett. **80**, 1102 (1998); W. D. Bragg, V. A. Markel, W. Kim, K. Banerjee, M. R. Young, J. G. Zhu, R. L. Armstrong, V. M. Shalaev, and Z. C. Ying, J. Opt. Soc. Am. B (to be published).

[41] H. Zhu and R. S. Averback, Philos. Mag. Lett. **73**, 27 (1996).

[42] S. E. Rorak, A. Lo, R. T. Skodje, and K. L. Rowlen, in *Nanostructured Materials: Clusters, Composites, and Thin Films*, edited by V. M Shalaev and M. Moskovits (American Chemical Society, Washington DC, 1998), pp. 152–168.